Heliyon 9 (2023) e13817

Contents lists available at ScienceDirect

Heliyon

journal homepage: www.cell.com/heliyon

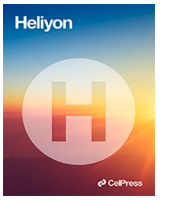

Research article

Enhancing pseudocapacitive properties of cobalt oxide hierarchical nanostructures via iron doping

Asab Fetene Alem [a], Ababay Ketema Worku [a,*], Delele Worku Ayele [a,b,***], Nigus Gabbiye Habtu [d], Mehary Dagnew Ambaw [c], Temesgen Atnafu Yemata [d,**]

[a] Bahir Dar Energy Center, Bahir Dar Institute of Technology, Bahir Dar University, Bahir Dar, P.O. Box 26, Ethiopia
[b] Department of Chemistry, College of Science, Bahir Dar University, P.O. Box 79, Bahir Dar, Ethiopia
[c] Department of Industrial Chemistry, College of Science, Bahir Dar University, P.O. Box 79, Bahir Dar, Ethiopia
[d] Faculty of Chemical and Food Engineering, Bahir Dar Institute of Technology-Bahir Dar University, Bahir Dar, P.O. Box 26, Ethiopia

ARTICLE INFO

Keywords:
Iron
Supercapacitor
Co-precipitation method
Cobalt oxide nanoparticles

ABSTRACT

Through co-precipitation and post-heat processing, nanostructured Fe-doped Co_3O_4 nanoparticles (NPs) were developed. Using the SEM, XRD, BET, FTIR, TGA/DTA, UV–Vis, and techniques were examined. The XRD analysis presented that Co_3O_4 and Co_3O_4 nanoparticles that had been doped with 0.25 M Fe formed single cubic phase Co_3O_4 NPs with average crystallite sizes of 19.37 nm and 14.09 nm, respectively. The as prepared NPs have porous architectures via SEM analyses. The BET surface areas of Co_3O_4 and 0.25 M Fe-doped Co_3O_4 NPs were 53.06 m^2/g and 351.56 m^2/g, respectively. Co_3O_4 NPs have a band gap energy of 2.96 eV and an extra sub-band gap energy of 1.95 eV. Fe-doped Co_3O_4 NPs were also found to have band gap energies between 2.54 and 1.46 eV. FTIR spectroscopy was used to determine whether M–O bonds (M = Co, Fe) were present. The doping impact of iron results in the doped Co_3O_4 samples having better thermal characteristics. The highest specific capacitance was achieved using 0.25 M Fe-doped Co_3O_4 NPs at 5 mV/s, which corresponding to 588.5 F/g via CV analysis. Additionally, 0.25 M Fe-doped Co_3O_4 NPs had energy and power densities of 9.17 W h/kg and 472.1 W/kg, correspondingly.

1. Introduction

Energy storage systems for clean and renewable energy have been developed as a result of the energy crisis and environmental pollution. Global warming and severe energy difficulties are currently becoming important issues [46,77]. This predicament has sparked researchers' efforts to create energy storage systems that are clean, green, sophisticated, and effective, like fuel cells, batteries, and supercapacitors [2,21]. In that case, batteries and electrochemical capacitors known as supercapacitors are the best candidates for the impending energy crisis. Rechargeable batteries are able to store electrical energy based on electrochemical redox reactions as positive and negative electrodes [60]. Moreover, after renewable energy generation, aqueous rechargeable cells are the practical and secure option for power storage [35,65,76]. As a result extensive analysis and researches are currently underway to develop a new,

* Corresponding author.
** Corresponding author.
*** Corresponding author. Department of Chemistry, College of Science, Bahir Dar University, P.O. Box 79, Bahir Dar, Ethiopia.
E-mail addresses: workuketema91@gmail.com (A.K. Worku), delelewww@gmail.com (D.W. Ayele), atnafutemesgen16@gmail.com (T.A. Yemata).

https://doi.org/10.1016/j.heliyon.2023.e13817
Received 31 October 2022; Received in revised form 8 February 2023; Accepted 14 February 2023
Available online 17 February 2023
2405-8440/© 2023 The Authors. Published by Elsevier Ltd. This is an open access article under the CC BY-NC-ND license (http://creativecommons.org/licenses/by-nc-nd/4.0/).

environmentally friendly, high-specific capacity and energy density with improved cyclic ability for a cost-effective energy storage materials [21,23,75]. To date, supercapacitor is the most promising new energy storage technology due to its excellent charge and discharge capabilities, long cycle life, and potential to transfer more power than conventional batteries [5]. Additionally, these advantageous energy storage devices have high energy density for hybrid electric vehicles [28,42,48,57,67,84]. Due to their extraordinary qualities, supercapacitors are excellent choices for usage in a variety of industrial, hybrid cars, mobile devices, electronic devices, and memory backup's energy storage systems [15,80].There are two categories of supercapacitors: electric double-layer capacitors (EDLC) and pseudocapacitors [17,59]. These different categories differ on the basis of the charge storage mechanisms [30,43,69,86]. As a pseudocapacitors electrode materials, transition metal oxides mainly include RuO_2, MnO_2, and Co_3O_4 [13,49,79, 82,85]. RuO_2 is regarded as the best pseudocapacitors electrode material due to its high theoretical capacity and rapid Faraday redox reaction [34,44,51]. However, its high price and environmental toxicity seriously limit its application in supercapacitor application [32,55,64]. Recently, among different types of transition metal oxides,Co_3O_4 has been increasing interest in the use of as an electrochemical material for pseudocapacitors due to its high theoretical capacitance value of 3650 F/g, excellent reversible redox reaction, due to its environmental friendliness, low cost and special microstructure and morphology [4,47,72,73]. However, the capacitance in real-world applications differs greatly from that in theory. One of the causes is that Co_3O_4 poor capacitance and cycle efficiency result from the material's significant volume expansion and contraction, low conductivity, and high particle aggregation [50,72,73]. Hence,Co_3O_4 nanoparticles (NPs) can be prepared via several approaches such as the hydrothermal [56], sol-gel method [61], thermal decomposition [25], co-precipitation [33,78], spray pyrolysis [11] and solvothermal methods [10].However, these methods are expensive, require complex equipment and take a long time to prepare [53,58]. Among these, co-precipitation approach, has the benefit of being quick, affordable, and simple to control throughout preparations [12,83]. Hence the nanoparticle properties and electrochemical performance may be varying with experimental parameters like synthesized method, concentration, precursor materials, reaction time, temperature and solvent. Numerous research have reported on the electrochemical activity of electrode materials based on transition metal oxides [45]. Reference [19] examined that Mn-doped Co_3O_4 microspheres using a solvothermal method and have obtained a good specific capacitance of 773 F/g in 2 M KOH aqueous solution at 1 A/g. Similarly, Ali and Khalid [7] examined that 6% Cr-doped Co_3O_4 nanoflower prepared using a hydrothermal method had a higher specific capacitance value of 1283 F/g at a 5 mV/s scan rate, which is 67% higher than pure Co_3O_4 (860 F/g). Similarly, Ali, Khalid, and Nabi et al. [8,9], reported that 5% Ce (1–7%) doped Co_3O_4 nanostructures made of nano flakes synthesized via a simple hydrothermal method showed a superior specific capacitance value of 1309.6 F/g, which is 40% higher than pure Co_3O_4 another researchers, Uma Sudharshini et al. and Khalid et al. [39,81] the successful synthesis of 5% Mo-doped Co_3O_4 porous NPs with various molybdenum concentrations using a straightforward sol-gel process, which demonstrated excellent specific capacitance of 858.09 F/g at a scan rate of 5 mV/s and good conductivity. Hence, according to the above all findings, different doping material holds ideal input for practical application of supercapacitors.

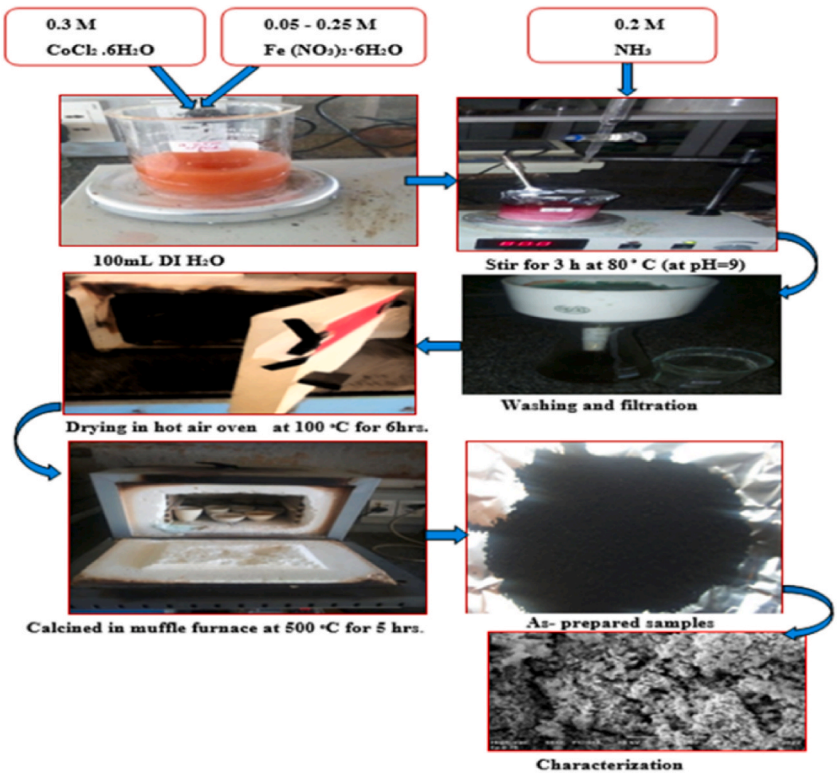

Fig. 1. Preparation of Fe-doped Co_3O_4 NPs using co-precipitation technique.

Recently, research has been published on the preparation of Co_3O_4 nanomaterials with metal dopants such as Ag, Sn, Sb, Cu, Fe, Cr, Mo, Ru, Ni, Mn, and Mo for different applications. Thus, according to the literature survey, it is found that Fe-doped Co_3O_4 NPs were mostly used as photocatalytic activity/electrolytes, biosensors, gas sensors [74]. Moreover, in the literature review, there are only a few reports on Fe-doped Co_3O_4 NPs for supercapacitor applications synthesized via co-precipitation technique. Hence, in this article Fe-doped Co_3O_4 NPs for supercapacitor applications were synthesized through a co-precipitation method with post-heat treatment.

2. Materials and methods

2.1. Materials

All utilized chemicals and reagents were of analytical grade and were not further purified. From chemical markets, we received $CoCl_2$. $6H_2O$, 99.9% (cobalt chloride hexahydrate), NH_3, 99.2% (ammonia solution), and iron (II) nitrate hexahydrate (Fe $(NO_3)_2 6H_2O$, 99.9%).To make the solutions, distilled water was used.

2.2. Fe-doped Co_3O_4 NPs synthesis

A simple co-precipitation method was used to create iron doped-Co_3O_4 NPs. Cobalt chloride ($CoCl_2 . 6H_2O$) hexahydrate (0.3 M) and the desired mole of (0.05, 0.1, 0.15, 0.2, and 0.25 M) iron (II) nitrate hexahydrate (Fe $(NO_3)_2 \cdot 6H_2O$) were dissolved in 100 mL of distilled water for the usual production of Fe-doped Co_3O_4 NPs. The resultant mixture was then agitated for 3 h at 80 °C using a magnetic stirrer. By gradually adding 0.2 M NH_3 solution to the mixture of Fe $(NO_3)_2 . 6H_2O$ and $CoCl_2 . 6H_2O$, the pH of the mixture was brought to 9. Following that, both items were filtered and repeatedly cleaned with distilled water and ethanol. Additionally, the samples were dried for 6 h in an oven at 100 °C to remove any remaining water and organic contaminants. The products were then calcined at 500 °C for 4 h in a muffle furnace. Un-doped Co_3O_4 was made using a similar technique. Fig. 1 provides a detailed schematic representation of the Co-precipitation developed Fe-doped Co_3O_4 NPs.

2.3. Characterization

Using a Fourier transform infrared spectrometer (FT-IR, 6660 (JASCO MODEL)) in the wavenumber range of 4000–500 cm^{-1}, the functional groups of nanoparticles were examined. The transmittance mode was used for the functional groups analysis, and KBr pellets were used for sample analysis. The nanoparticle dry powder was mixed with KBr, milled and pressed into disk. The crystal structure and the phase purity of the nanoparticles has been analyzed by powder X-ray diffraction (MAXima-X XRD-7000, SHIMADZU) technique. The advance Cu- Kα with wavelength of 0.154 nm, Bruker's X-ray powder diffractometer was used for structural analysis. The nanoparticle powder samples were characterized in the 2Θ range of 10–60°. SEM (INSPECT F50) were used to analyze the morphology of the produced nanomaterials at various magnification scales. TGA/DTA analysis was used to determine the thermal characteristics. The UV–Vis, Lambda35 (PerkinElmer) spectrophotometer was used to examine the optical properties of the created nanoparticles in the wavelength range of 250–500 nm. With Quanta chrome Nova Win, the Brunner-Emmet-Teller (BET) Surface Area of nanoparticles was calculated (Quanta chrome Instruments version 11.0).

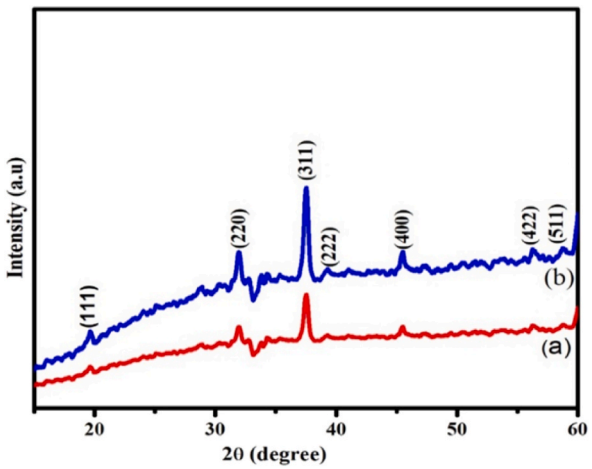

Fig. 2. XRD pattern of (a) Pure Co_3O_4 nanoparticles, and (b) 0.25 M Fe-doped Co_3O_4 NPs.

3. Results and discussion

3.1. XRD analysis

The crystal structures and phases of as-prepared pure Co_3O_4 and Fe-doped Co_3O_4 NPs were investigated using the XRD analysis (Fig. 2). The XRD technique was used to evaluate all of the as-prepared samples. The diffraction peaks at 19.68°, 31.89°, 37.47°, 39.29°, 45.5°, 55.89°, and 59.11° correspond to the cubic Co_3O_4 crystalline planes (111), (220), (311), (222), (400), (422), and (511), respectively. As a result, the XRD peaks and the JCPDS data are in good agreement (JCPDS card no. 09–0418) [41,54].

Doping has no effect on the cubic structure of the as prepared material, however it affects the samples' crystallinity by increasing the intensities and peak positions. The average crystal size of pure Co_3O_4 NPs and 0.25 M Fe-doped Co_3O_4NPs was found using the Debye-Scherer Equation (1) [24].

$$D = \frac{k\lambda}{\beta \cos \theta} \tag{1}$$

where, D, k, ʎ, and θ represents crystal size, Debye–Scherer constant, wavelength and diffraction angle, correspondingly [6]. For 0.25 M Fe–Co_3O_4 NPs and pure Co3O4 it was discovered that the average crystal size was equal to 19.37 and 14.09 nm, correspondingly (Table 1). The outcome indicated that Fe doping reduced particle size. Because of their high surface-to-volume ratio and great capacity for charge storage, tiny crystals have a small value [8,9].

3.2. Morphology analysis

SEM morphological analysis of pure Co_3O_4 and 0.25 M Fe-doped Co_3O_4 NPs at various magnification scales were illustrated in Fig. 3(a–b). At 20 μm, SEM morphologies in Fig. 3a revealed that the particles have a porous structure with tiny spherical grains. In contrast, Fig. 3b at a magnification of 10 μm, demonstrates more porous structure NPs. This implied that the presence of iron changed the surface morphology of Co_3O_4 NPs. The SEM data show a substantial difference in morphology between pure and Fe-doped Co_3O_4 NPs, demonstrating that the concentration of Fe used for doping has a significant impact on the morphology of Co_3O_4 NPs. As a result, 0.25 M Fe-doped Co_3O_4 NPs exhibit higher porosity and greater particle dispersion than Co_3O_4 NPs, which is a potential characteristic to improve the catalytic performance of the nanoparticles as generated [68].

3.3. Analysis of surface area

The BET analysis was used to calculate the specific surface areas, pore volume, and pore radius of Co_3O_4 and Fe-doped Co_3O_4, as shown in Table 2 [3,31]. For Co_3O_4 and 0.25 M Fe-doped Co_3O_4 NPs, the BET specific surface were calculated to be 53.066 m^2/g, and 351. 560 m^2/g, correspondingly. In addition, Co_3O_4 and 0.25 M Fe-doped Co_3O_4 NPs showed a pore radii of 13.85 Å and 13.24 Å, respectively. The 0.25 M Fe-doped Co_3O_4 NPs greater surface area and pore volume can create more room and improve electrochemical surface reactions. The outcome is a higher concentration of electrochemically active sites, a bigger area at the electrolyte-ion interface, and a shorter diffusion path enabling rapid ion diffusion, all of which contribute to excellent performance [20]. Hence, a greater BET surface area helps the electrode to store and transport electrons and ions, creating more active sites and a higher electrochemical potential [62]. Through this study, it was discovered that the presence of iron ions caused changes in the Co_3O_4 NPs surface area, pore volume, and pore size [29].

3.4. FT-IR analysis

Fe-doped and un-doped Co_3O_4 NPs FTIR spectra were captured in the 4000-500 cm^{-1} region. The FTIR spectra of Co_3O_4 and Fe-doped Co_3O_4 NPs at various doping levels are shown in Fig. 4. The band at roughly 3427 cm^{-1} corresponds to the O–H stretching vibration of water molecules, while the smaller band at approximately 1619 cm^{-1} may be caused by the O–H stretching and bending modes of water molecules. The intensity of the OH stretching vibration absorption peak is reduced with adding iron ions, to Co_3O_4 NPs. The peaks between 3400 and 2900 cm^{-1} were caused by carbonaceous chemicals and O–H stretching, respectively [66]. Additionally, the band roughly between 1379 and 1110 cm^{-1} matches the O–H–Co stretching vibration. Due to the addition of iron ion, the band shifted slightly towards the higher wavenumber region. Finally, the characteristic peaks at 620 cm^{-1} and 570 cm^{-1} are connected to the stretching vibrations of the metal-oxygen(M–O) bond, which supports the spinel structure of Co_3O_4 NPs [26]. Moreover, the FTIR spectra investigation are well matching with others findings [63,70]. According to FTIR result the peak intensity raised with increasing iron doping levels, which also improved the crystallinity of the NPs. The existence of optical vibrational modes reveals the formation of

Table 1
XRD determination of pure Co_3O_4 and 0.25 M Fe-doped Co_3O_4 NPs.

Nanoparticles	2θ	FWHM	D (nm)
pure Co_3O_4	31.63799	0.42607	19.37945
Fe-doped Co_3O_4	31.63568	0.58583	14.09445

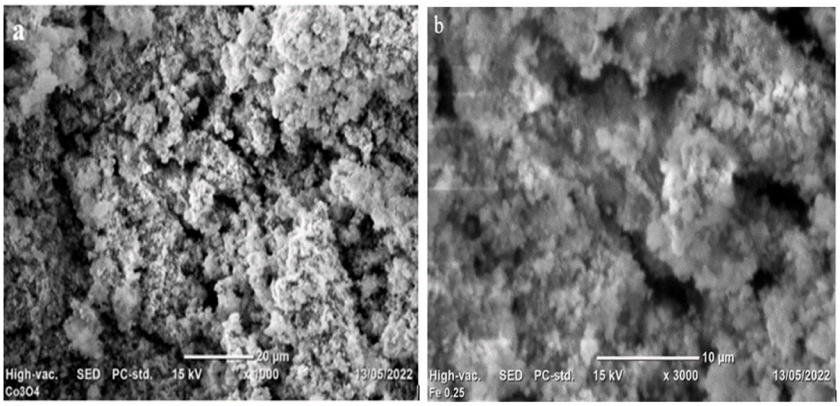

Fig. 3. SEM pictures of (a) Pure Co_3O_4 nanoparticles at 20 µm (b) 0.25 M Fe-doped Co_3O_4 NPs at 10 µm.

Table 2
BET pore-volume, pore radius and specific surface area of Co_3O_4 and Fe-doped Co_3O_4 NPs.

Samples	BET Surface area (m^2/g)	Pore volume (cc/g)	Pore radius (Å)
Co_3O_4	53.066	0.07425	13.85
0.25 M Fe–Co_3O_4	351.560	0.1191	1 3.24

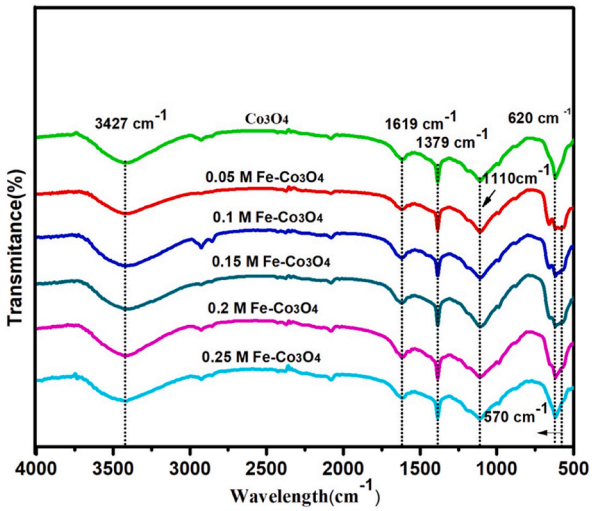

Fig. 4. FTIR spectra of Co_3O_4, Fe-doped Co_3O_4 (0.05 M), Fe-doped Co_3O_4 (0.1 M), Fe-doped Co_3O_4 (0.15 M), Fe-doped Co_3O_4 (0.2 M), Fe-doped Co_3O_4 (0.25 M) NPs.

cobalt oxide in NPs.

3.5. UV–Vis analysis

UV–Vis analyses were carried out to examine the optical characteristics of as-prepared nanoparticles. Fig. 5 shows the UV–visible spectra of Co3O4 and Fe-doped Co3O4 nanoparticles. The analysis displayed that Fe doping concentration affects the absorbance values in UV–Visible spectra [18]. Another notable aspect of the absorption spectrum is the presence of two pronounced absorption edges in the visible region in all observed spectra, which are ascribed to the ligand-to-metal charge transmission result of ($O^{2-} \rightarrow Co^{2+}$) and ($O^{2-} \rightarrow Co^{3+}$) in Co_3O_4 [52]. The absorption bands of Fe-doped Co_3O_4 vary with a change in the concentration of iron. The optical band gap of un-doped Co_3O_4 and Fe-doped Co_3O_4 (0.05–0.25 M) sample were calculated using Tauc relation from Eq. (2) [16,63].

$$(\alpha h\nu)^n = A\left(h\nu - E_g\right) \tag{2}$$

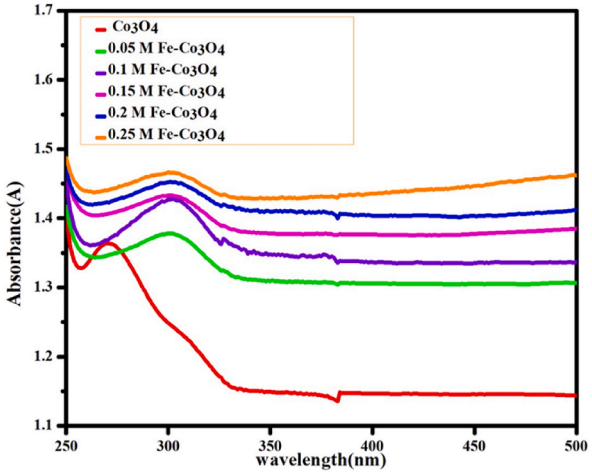

Fig. 5. UV–Visible spectrum of Co_3O_4, Fe-doped Co_3O_4 (0.05 M), Fe-doped Co_3O_4 (0.1 M), Fe-doped Co_3O_4 (0.15 M), Fe-doped Co_3O_4 (0.2 M) and Fe-doped Co_3O_4 (0.25 M) NPs.

where, hv is photon energy, A is constant, E_g is the bandgap energy α is absorption coefficient, and n is the constant [37]. Tauc plot of Co_3O_4, and Fe doped Co_3O_4 (0.05, 0.1, 0.15, 0.2 and 0.25 M) NPs were calculated by extrapolating the linear part of these plots of $(\alpha h\nu)^2$ axis to ($h\nu$) axis (Fig. 6). The bandgap energy variation is observed due to the addition Fe ions (Table 3). The maximum bandgap energy for Co_3O_4 NPs is assigned to the valence to conduction band excitation of ($O^{2-} \rightarrow Co^{2+}$ charge transfer), while the minimum band gap is assigned to the $O^{2-} \rightarrow Co^{3+}$ charge transfer at 0.25 M Fe-doped Co_3O_4 NPs where Co^{3+} ions are located below the conduction band; due to this impurity energy levels are created in the bandgap region. In contrast, Fe contributes to hole generation and increases its role with the number of charge carriers (holes) that contribute to conductivity of Co_3O_4 NPs.

3.6. Thermal analysis

Through the use of TGA and DTA, the thermal characteristics of un-doped Co_3O_4 and Fe-doped Co_3O_4 NPs were examined. The sample mass was approximately 10 mg, and it was heated in an environment of air at a rate of 20 °C per minute in a corundum crucible between 25 °C and 900 °C [36]. The TGA and DTA curves of Fe-doped Co_3O_4 and Co_3O_4 NPs are shown in Fig. 7, respectively. The TGA profiles of Co_3O_4 NPs and Fe-doped Co_3O_4 NPs show two stages of weight reduction. The first weight loss of 0.37 mg for Co_3O_4 NPs between 25 and 262 °C and the corresponding endothermic peak at 135 °C include the loss of absorbed water in the sample [83]. The degradation of the precursor materials or remaining organic ligands was associated to the second mass losses (1.54 mg) in the range of 262–599 °C, with corresponding DTA curves at 342 and 506 °C [1]. The final mass loss of 8.09 mg from the initial weight of 10 mg at 900 °C is comparable to a mass loss of 19.1% (Fig. 7a.) The endothermic peak that corresponds to this temperature may be due to the loss of physically adsorbed water as the first mass loss of 0.41 mg is observed on the 0.05 M Fe–Co_3O_4 NPs TGA curve between 25 and 279 °C (Fig. 7b). The second range of mass losses (1.15 mg) in the range of 279–598 °C were attributed to the breakdown of leftover organic ligands and the DTA curves at 339 and 509 °C. The final mass loss of 8.44 mg from the initial weight of 10 mg at 900 °C is 15.6% mass loss (Fig. 7b). Additionally, the endothermic peak that corresponds to the first mass loss of 0.89 mg between 25 and 300 °C on the 0.1 M Fe–Co_3O_4 NPs TGA curve may be produced by the loss of physically adsorbed water (Fig. 7c). The second range (0.19 mg) mass losses in the range of 300–475 °C, with corresponding DTA curves at 507 and 574 °C, were linked to the breakdown of the remaining organic ligands. The final mass loss from the starting weight of 10 mg is 8.92 mg, or 10.8%, when heated to 900 °C (Fig. 7c). The endothermic peak at 106 °C that it corresponds to the loss of physically adsorbed water, as shown by the first mass loss of 0.9 mg between 25 and 296 °C on the 0.15 M Fe-doped Co_3O_4 NPs TGA curve (Fig. 7d) [38]. The breakdown of lingering organic ligands was linked to the second range of mass losses (0.14 mg), which occurred in the range of 296–486 °C, using matching DTA curves at 415 and 458 °C. However, after 495 °C, there is no change in the TGA/DTA patterns of 0.15 M Fe–Co_3O_4 NPs. The final mass loss of 8.96 mg from the initial weight of 10 mg at 900 °C is comparable to a mass loss of 10.4% (Fig. 7d). Thermal testing demonstrates that the interaction between the Fe and Co_3O_4 NPs gives rise to the material's noticeably different thermal characteristics. As a result, Fe-doped Co_3O_4 NPs display significantly higher thermal stability as the dopant concentration increases (Table 4) [14].

3.7. Cyclic voltammetry (CV) analysis

Cyclic voltammetry (CV) was used for electrochemical investigations. To evaluation the capacitance of un-doped Co_3O_4 and 0.25 M Fe-doped Co_3O_4 NPs used this analysis. Fig. 8a–c shows the findings of the CV curve that was recorded in the potential range of −0.1 to + 0.6 V vs Ag/Ag Cl at scan rates of 5, 10, 20, 50, and 100 mV/s in 0.1 M KOH. Wide and distinct redox peaks seen from nonlinear CV curves which support the Fe-doped Co_3O_4 NPs pseudo-capacitance property. When the scanning rate was increased from 5 to 100 mV/s, the strong redox peaks were still visible, showing good reversibility of redox reactions [22].

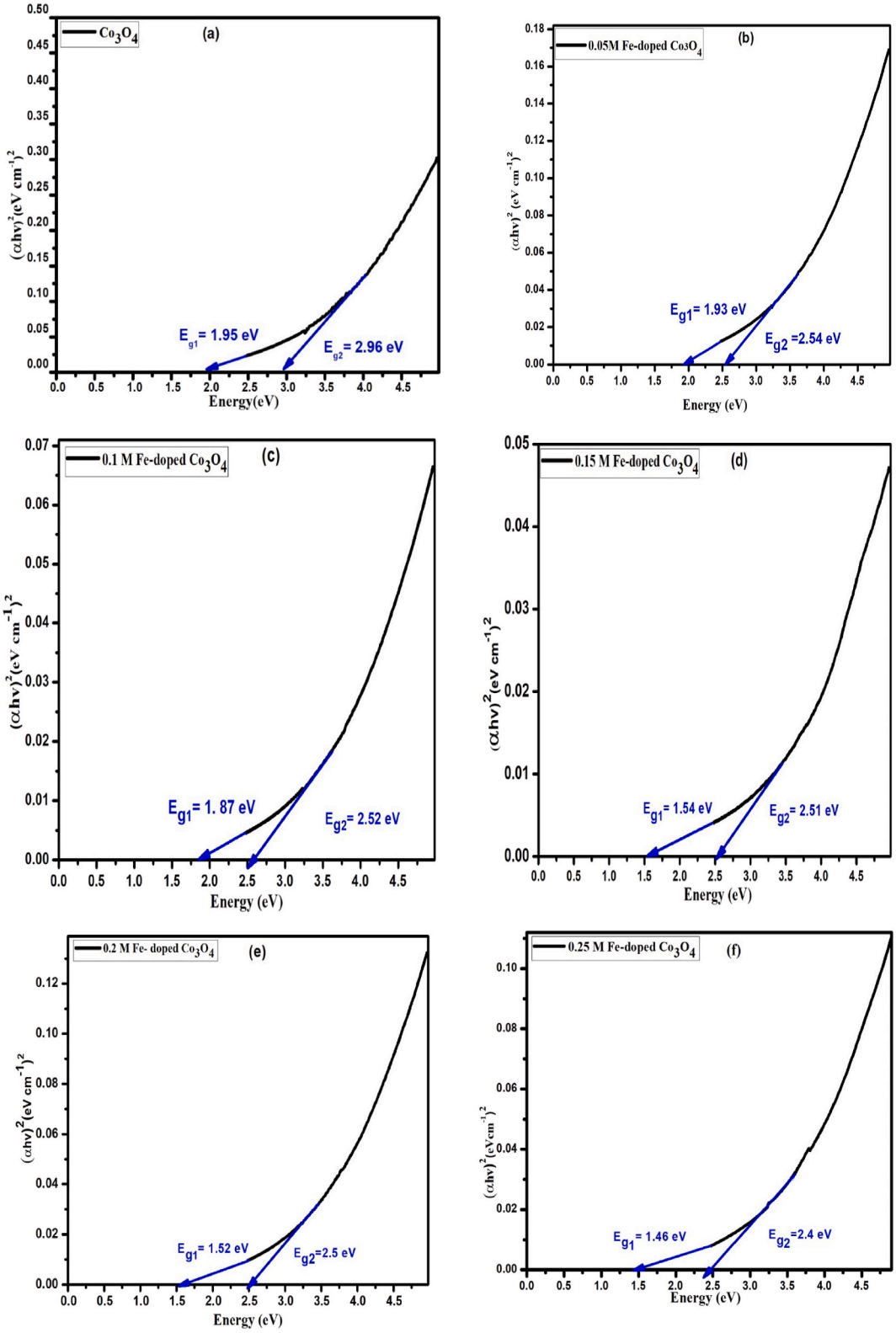

Fig. 6. Tauc plot of (a) pure Co_3O_4, (b) Fe-doped Co_3O_4 (0.05 M), (c) Fe-doped Co_3O_4 (0.1 M), (d) Fe-doped Co_3O_4 (0.15 M), (e) Fe-doped Co_3O_4 (0.2 M), (f) Fe -doped Co_3O_4 (0.25 M) nanoparticles.

Table 3
Co_3O_4 and Fe-doped Co_3O_4 NPs optical band gap values.

Samples	Eg_1 (eV)	Eg_2 (eV)
Co_3O_4	1.95	2.96
Fe-doped Co_3O_4 (0.05 M)	1.93	2.54
Fe-doped Co_3O_4 (0.1 M)	1.87	2.52
Fe-doped Co_3O_4 (0.15 M)	1.54	2.51
Fe-doped Co_3O_4 (0.2 M)	1.52	2.50
Fe-doped Co_3O_4 (0.25 M)	1.46	2.40

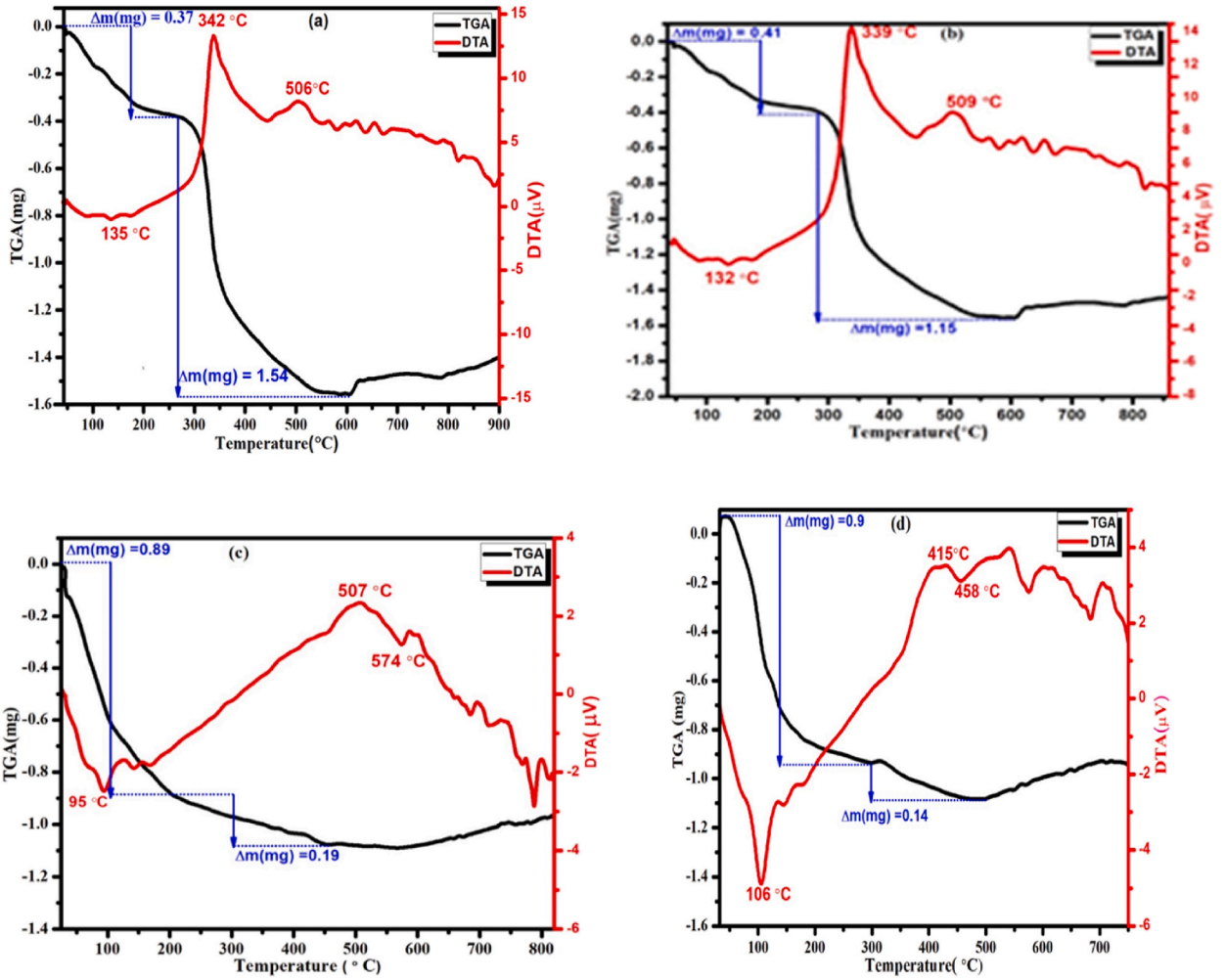

Fig. 7. TGA and DTA curve of (a) Co_3O_4 nanoparticles, (b) Fe-doped Co_3O_4 (0.05 M) nanoparticles, (c) Fe-doped Co_3O_4 (0.1 M) nanoparticles, (d) Fe-doped Co_3O_4 (0.15 M) nanoparticles.

Hence, Eq. (3) was used to estimate the specific capacitance of pure Co_3O_4 and 0.25 M Fe-doped Co_3O_4 nanoparticles determined from CV curves [8,9].

$$Cs = \frac{\int_{v1}^{V2} IdV}{mv\Delta V} \tag{3}$$

where Cs, I, V_1, V_2, v, and m represents specific capacitance (F/g), oxidation/reduction current for a given voltage V (v), lower potential limit, upper potential limit, scan rate (v/s) and mass of the electrode (g), respectively. At a scan rate of 5 mV/s, the Co_3O_4 electrode only displays a high specific capacitance value of 393.6 F/g. These values are comparable with literature-reported values

Table 4
Summary of TGA-DTA analysis results.

Samples	Temperature range (°C)	Endothermic peak (°C)	1st stage weight loss (TGA)		2nd stage weight loss (TGA)		Total weight loss (%)	Decomposition temperature (°C) in the DTA curve
			Temperature range °C	weight loss (mg)	Temperature range °C	Weight loss (mg)		
Co_3O_4	25–900	135	25–262	0.37	262–599	1.54	19.1	342 and 506
Fe–Co_3O_4 (0.05 M)	25–900	132	25–279	0.41	279–598	1.15	15.6	339 and 509
Fe– Co_3O_4 (0.1 M)	25–900	95	25–300	0.89	300–475	0.19	10.8	507 and 574
Fe–Co_3O_4 (0.15 M)	25–900	106	25–296	0.9	296–486	0.14	10.4	415 and 458

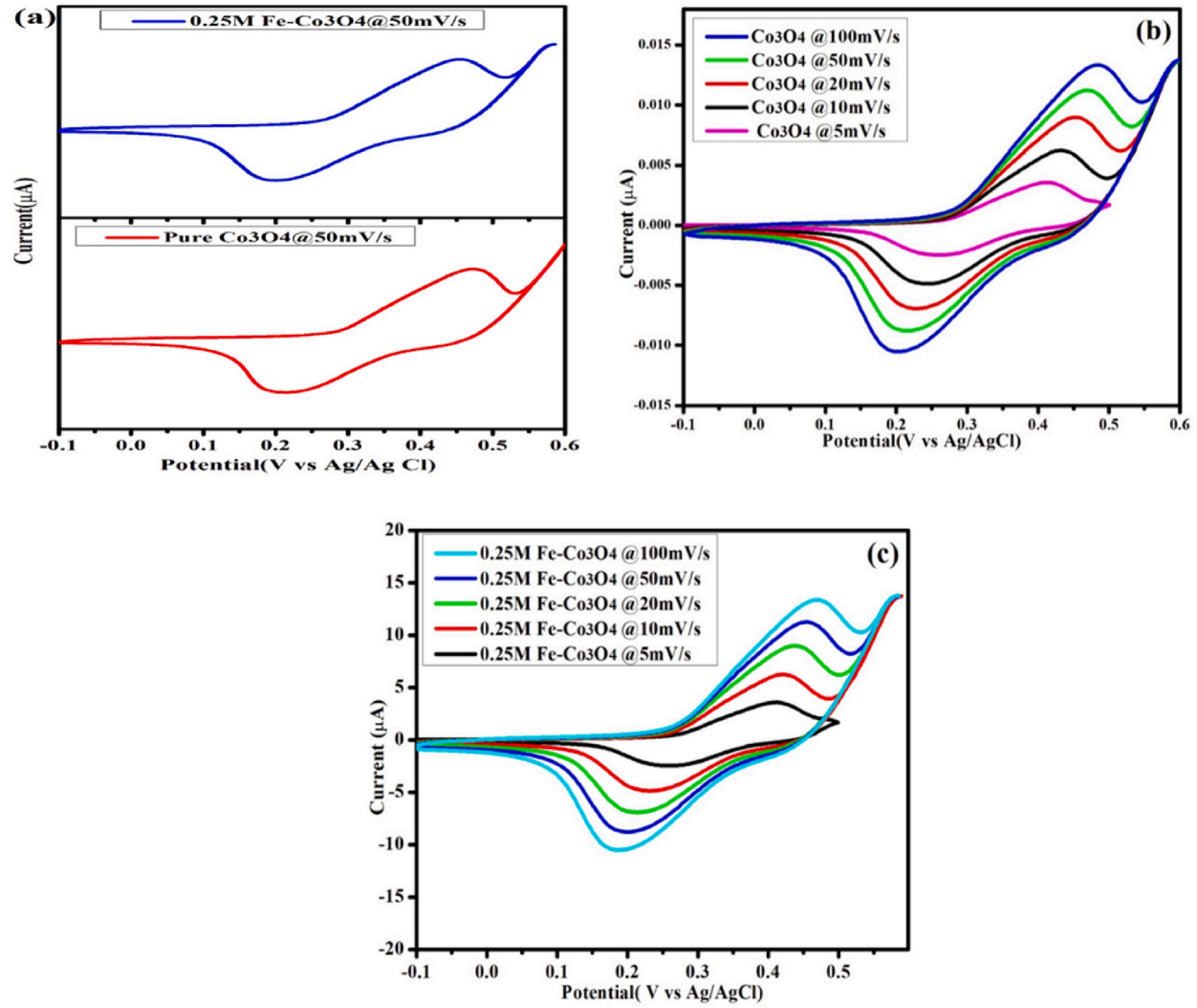

Fig. 8. CV Curve of (a) Co_3O_4 and 0.25 M Fe-doped Co_3O_4 nanoparticles at 50 mV/s nanoparticles at different scan rates, (b) Co_3O_4 nanoparticles at different scan rates, and (c) 0.25 M Fe-doped Co_3O_4 nanoparticles at different scan rates.

Table 5
The specific capacitance values of pure Co_3O_4 and Fe-doped Co_3O_4 NPs.

Scan rate (mV/s)	Specific capacitance(F/g) (Co_3O_4)	Specific capacitance (F/g) (0.25 M Fe-doped Co_3O_4)
5	393.6	588.5
10	328.7	523.1
20	230.6	395.7
50	143.1	329.4
100	109.8	261.6

[40]. However, 0.25 M Fe-doped Co_3O_4 nanoparticles electrodes exhibits a high Specific Capacitance value of 588.5 F/g at a scan rate of 5 mV/s (Table 5). Notably, this particular capacitance value is higher than values previously reported in the literature.

3.8. Power density and energy density analysis

The power and energy density of the as-prepared materials were obtained according to Eqs. (4) and (5) [27,71].

$$E = \frac{1}{2} C(\Delta V)^2 \Big/ 3.6 \tag{4}$$

$$P = 3600\, E/\Delta t \tag{5}$$

where C is the capacitance of the electrode (F/g), E is the energy density (Wh/kg), and ΔV (V), is the potential window of device, P is the power density (W/kg), Δt (s) is the discharge time. At a power density of 160.4 W/kg, the Co_3O_4 NPs had a maximum energy density of 6.69 W h/kg. In contrast, 9.17 W h/kg of 0.25 M Fe doped Co_3O_4 NPs had a power density of 472.1 W/kg. In this study, Co_3O_4 and 0.25 M Fe-doped Co_3O_4 NPs had a greater power density than those previously reported in the literature [29].

4. Conclusion

Using a co-precipitation synthesis technique by varying the concentrations of iron, Fe-doped Co_3O_4 NPs for supercapacitor applications were investigated. Through the use of FTIR, XRD, TGA/DTA, SEM, UV-VIS, BET and CV analyses, the as-prepared materials were characterized. XRD analysis showed that an average particle size of 19.37 and 12.98 nm for Co_3O_4 and Fe-doped Co_3O_4 NPs, respectively. Morphological analysis of Co_3O_4, and 0.25 M Fe-doped Co_3O_4 showed porous structures. The BET surface areas of Co_3O_4 and 0.25 M Fe-doped Co_3O_4 NPs were 53.06 m^2/g and 351.56 m^2/g, respectively. Co_3O_4 NPs have a band gap energy of 2.96 eV and an extra sub-band gap energy of 1.95 eV. Additionally, the band gaps of Fe-doped Co_3O_4 NPs were between 2.4 and 2.54 eV for all samples, with a second sub-band with an energy range between 1.46 and 1.93 eV. FTIR spectroscopy was used to examine the formation of M–O bonds. The doping impact of iron results in the Co_3O_4 samples having better thermal characteristics. In order to conduct the electrochemical measurements, a CV analysis in a 0.1 M KOH electrolyte solution was used. The CV test showed that, at a scan rate of 5 mV/s, the samples of Co_3O_4 and 0.25 M Fe-doped Co_3O_4 NPs displayed the greatest specific capacitance values of 393.6 F/g and 588.5 F/g, respectively. Additionally, the Co_3O_4 NPs and 0.25 M Fe-doped Co_3O_4 NPs energy and power densities were 6.69 W h/kg, 160.4 W/kg, and 9.17 W h/kg, 472.1 W/kg, respective. These findings point to its possible use in energy storage technology.

Author contribution statement

Asab Fetene Alem, Ababay Ketema Worku: Conceived and designed the experiments; Performed the experiments; Analyzed and interpreted the data; Wrote the paper. Delele Worku Ayele, Nigus Gabbiye Habtu, Temesgen Atnafu Yemata: Analyzed and interpreted the data; Contributed reagents, materials, analysis tools or data; Wrote the paper. Mehary Dagnew Ambaw: Conceived and designed the experiments; Wrote the paper.

Funding statement

This research did not receive any specific grant from funding agencies in the public, commercial, or not-for-profit sectors.

Data availability statement

Date will be made available on request.

Declaration of interest's statement

The authors declare no conflict of interest.

Acknowledgments

The authors would like to thank faculty of Chemical and Food Engineering laboratory technicians for their chemical and characterization support.

References

[1] M. Aadil, S. Zulfiqar, H. Sabeeh, M.F. Warsi, M. Shahid, I.A. Alsafari, I. Shakir, Enhanced electrochemical energy storage properties of carbon coated Co3O4 nanoparticles-reduced graphene oxide ternary nano-hybrids, Ceram. Int. 46 (11) (2020) 17836–17845, https://doi.org/10.1016/j.ceramint.2020.04.090.
[2] M. Aadil, S. Zulfiqar, M. Shahid, S. Haider, I. Shakir, M.F. Warsi, Binder free mesoporous Ag-doped Co3O4 nanosheets with outstanding cyclic stability and rate capability for advanced supercapacitor applications, J. Alloys Compd. (2020), 156062, https://doi.org/10.1016/j.jallcom.2020.156062.
[3] M. Aadil, S. Zulfiqar, M.F. Warsi, P.O. Agboola, I. Shakir, M. Shahid, N.F. Al-Khalli, Mesoporous and macroporous Ag-doped Co3O4 nanosheets and their superior photo-catalytic properties under solar light irradiation, Ceram. Int. 47 (7) (2021) 9806–9817, https://doi.org/10.1016/j.ceramint.2020.12.121.
[4] S. Adhikari, S. Selvaraj, S.H. Ji, D.H. Kim, Encapsulation of Co3O4 nanocone arrays via ultrathin NiO for superior performance asymmetric supercapacitors, Small 16 (48) (2020) 1–13, https://doi.org/10.1002/smll.202005414.
[5] A.F. Alem, A.K. Worku, D.W. Ayele, T.A. Wubieneh, A. Abebaw Teshager, Tadele mihret kndie, B.T. Admasu, M.A. Teshager, A.A. Asege, M.D. Ambaw, M. A. Zeleke, A.K. Shibesh, T.A. Yemata, Ag doped Co3O4 nanoparticles for high-performance supercapacitor application, Heliyon (2023), e13286, https://doi.org/10.1016/J.HELIYON.2023.E13286.
[6] F. Ali, N.R. Khalid, E ff ect of calcination temperature on structural , morphological and electrochemical properties of Sn doped Co 3 O 4 nanorods, Ceram. Int. (2020), https://doi.org/10.1016/j.ceramint.2020.06.193.
[7] F. Ali, N.R. Khalid, Facile synthesis and properties of chromium - doped cobalt oxide (Cr-doped-Co3O4) nanostructures for supercapacitor applications, Appl. Nanosci. (2020), https://doi.org/10.1007/s13204-020-01266-5.
[8] F. Ali, N.R. Khalid, G. Nabi, A. Ul-Hamid, M. Ikram, Hydrothermal synthesis of cerium-doped Co3O4 nanoflakes as electrode for supercapacitor application, Int. J. Energy Res. 45 (2) (2021) 1999–2010, https://doi.org/10.1002/er.5893.
[9] F. Ali, N.R. Khalid, N.A. Niaz, G. Nabi, M.B. Tahir, M. Rafique, Novel Cr and Sn co-doped Co3O4 polygon-based electrode material for supercapacitor application, J. Mater. Sci. Mater. Electron. 32 (9) (2021) 11467–11477, https://doi.org/10.1007/s10854-021-05657-4.
[10] M. Aliofkhazraei, Handbook of nanoparticles, in: Handbook of Nanoparticles, 2015, https://doi.org/10.1007/978-3-319-15338-4.
[11] R.C. Ambare, S.R. Bharadwaj, B.J. Lokhande, Non-aqueous route spray pyrolyzed Ru:Co 3 O 4 thin electrodes for supercapacitor application, Appl. Surf. Sci. 349 (2015) 887–896, https://doi.org/10.1016/j.apsusc.2015.04.175.
[12] E. Arora, R. Chaudhary, S. Kumar, D. Kumar, Synthesis and characterization of copper doped cobalt oxide (Co3O4) by Co-precipitation method, Springer Proc. Phys. 178 (2017) 177–183, https://doi.org/10.1007/978-3-319-29096-6.
[13] N. B, V. Y, S. Abdul Razack, Enhanced formation of ruthenium oxide nanoparticles through green synthesis for highly efficient supercapacitor applications, Adv. Powder Technol. 31 (3) (2020) 1001–1006, https://doi.org/10.1016/j.apt.2019.12.026.
[14] T. Baidya, T. Murayama, P. Bera, O.V. Safonova, P. Steiger, N.K. Katiyar, K. Biswas, M. Haruta, Low-temperature CO oxidation over combustion made Fe- and Cr-doped Co3O4 catalysts: role of dopant's nature toward achieving superior catalytic activity and stability, J. Phys. Chem. C 121 (28) (2017) 15256–15265, https://doi.org/10.1021/acs.jpcc.7b04348.
[15] A. Borenstein, O. Hanna, R. Attias, S. Luski, Carbon-based composite materials for supercapacitor electrodes : a review, J. Mater. Chem.: Mater. Energy Sustain. 5 (2017) 12653–12672, https://doi.org/10.1039/C7TA00863E.
[16] J. Al Boukhari, L. Zeidan, A. Khalaf, R. Awad, Synthesis , characterization , optical and magnetic properties of pure and Mn , Fe and Zn doped NiO nanoparticles, Chem. Phys. (2018), https://doi.org/10.1016/j.chemphys.2018.07.046.
[17] B. Chameh, M. Moradi, S. Hajati, F.A. Hessari, Design and construction of ZIF(8 and 67) supported Fe3O4 composite as advanced materials of high performance supercapacitor, Phys. E Low-dimens. Syst. Nanostruct. 126 (2021), 114442, https://doi.org/10.1016/j.physe.2020.114442.
[18] H. Chen, W. Li, M. He, X. Chang, X. Zheng, Z. Ren, Vertically oriented carbon nanotube as a stable frame to support the Co0.85Se nanoparticles for high performance supercapacitor electrode, J. Alloys Compd. 855 (2021), https://doi.org/10.1016/j.jallcom.2020.157506.
[19] H. Chen, J. Wang, F. Liao, X. Han, Y. Zhang, C. Xu, L. Gao, Uniform and porous Mn-doped Co 3 O 4 microspheres: solvothermal synthesis and their superior supercapacitor performances, Ceram. Int. 45 (9) (2019) 11876–11882, https://doi.org/10.1016/j.ceramint.2019.03.070.
[20] L. Chen, Z. Song, G. Liu, J. Qiu, C. Yu, J. Qin, L. Ma, F. Tian, W. Liu, Synthesis and electrochemical performance of polyaniline-MnO2 nanowire composites for supercapacitors, J. Phys. Chem. Solid. 74 (2) (2013) 360–365, https://doi.org/10.1016/j.jpcs.2012.10.013.
[21] Y. Chen, W.K. Pang, H. Bai, T. Zhou, Y. Liu, S. Li, Z. Guo, Enhanced structural stability of nickel-cobalt hydroxide via intrinsic pillar effect of metaborate for high-power and long-life supercapacitor electrodes, Nano Lett. 17 (1) (2017) 429–436, https://doi.org/10.1021/acs.nanolett.6b04427.
[22] L. Cheng, M. Xu, Q. Zhang, G. Li, J. Chen, Y. Lou, NH4F assisted and morphology-controlled fabrication of ZnCo2O4 nanostructures on Ni-foam for enhanced energy storage devices, J. Alloys Compd. 781 (2019) 245–254, https://doi.org/10.1016/j.jallcom.2018.11.402.
[23] H.J. Choi, S.M. Jung, J.M. Seo, D.W. Chang, L. Dai, J.B. Baek, Graphene for energy conversion and storage in fuel cells and supercapacitors, Nano Energy 1 (4) (2012) 534–551, https://doi.org/10.1016/j.nanoen.2012.05.001.
[24] S. Das, C. Manoharan, M. Venkateshwarlu, P. Dhamodharan, Structural, optical, morphological and magnetic properties of nickel doped cobalt ferrite nanoparticles synthesized by hydrothermal method, J. Mater. Sci. Mater. Electron. 30 (22) (2019) 19880–19893, https://doi.org/10.1007/s10854-019-02355-0.
[25] S. Farhadi, M. Javanmard, G. Nadri, Characterization of cobalt oxide nanoparticles prepared by the thermal decomposition of [Co(NH3)5(H2O)](NO3)3 complex and study of their photocatalytic activity, Acta Chim. Slov. 63 (2) (2016) 335–343, https://doi.org/10.17344/acsi.2016.2305.
[26] M. Galini, M. Salehi, M. Behzad, Structural, magnetic and dielectric properties of Dy-doped Co 3 O 4 nanostructures for the electrochemical evolution of oxygen in alkaline media, J. Nanostruct. 8 (4) (2018) 391–403, https://doi.org/10.22052/JNS.2018.04.009.
[27] H. Gao, S. Cao, Y. Cao, Hierarchical Core-Shell Nanosheet Arrays with MnO2 Grown on Mesoporous CoFe2O4 Support for High-Performance Asymmetric Supercapacitors, 2017.
[28] Y.P. Gao, Z.B. Zhai, Q.Q. Wang, Z.Q. Hou, K.J. Huang, Cycling profile of layered MgAl2O4/reduced graphene oxide composite for asymmetrical supercapacitor, J. Colloid Interface Sci. 539 (2019) 38–44, https://doi.org/10.1016/j.jcis.2018.12.045.
[29] D. Guragain, S. Karna, J. Choi, R. Bhattarai, T.P. Poudel, R.K. Gupta, X. Shen, S.R. Mishra, Electrochemical Performance of Iron-Doped Cobalt Oxide Hierarchical Nanostructure, 2021.
[30] N.G. Habtu, A.K. Worku, D.W. Ayele, M.A. Teshager, Z.G. Workineh, Facile preparation and electrochemical investigations of copper-ion doped α-MnO2 nanoparticles, in: Lecture Notes of the Institute for Computer Sciences, Social-Informatics and Telecommunications Engineering, LNICST, 412 LNICST, 2022, pp. 543–553, https://doi.org/10.1007/978-3-030-93712-6_36.
[31] R. Hossain, V. Sahajwalla, Microrecycled Co3O4 from waste lithium-ion battery: synthesis, characterisation and implication in environmental application, J. Environ. Chem. Eng. (2022), 107858, https://doi.org/10.1016/j.jece.2022.107858.
[32] Y. Huang, S. Bao, J. Lu, Flower-like MnO2/polyaniline/hollow mesoporous silica as electrode for high-performance all-solid-state supercapacitors, J. Alloys Compd. 845 (2020), 156192, https://doi.org/10.1016/j.jallcom.2020.156192.
[33] M.R.S.A. Janjua, Synthesis of Co3O4 nano aggregates by Co-precipitation method and its catalytic and fuel additive applications, Open Chem. 17 (1) (2019) 865–873, https://doi.org/10.1515/chem-2019-0100.

[34] T.N. Jebakumar Immanuel Edison, R. Atchudan, Y.R. Lee, Facile synthesis of carbon encapsulated RuO2 nanorods for supercapacitor and electrocatalytic hydrogen evolution reaction, Int. J. Hydrogen Energy (2019) 2323–2329, https://doi.org/10.1016/j.ijhydene.2018.02.018.

[35] M. Jiang, N. Abushrenta, X. Wu, Y. Li, X. Sun, Investigation for the synthesis of hierarchical Co3O4@MnO2 nanoarrays materials and their application for supercapacitor, J. Mater. Sci. Mater. Electron. 28 (2) (2017) 1281–1287, https://doi.org/10.1007/s10854-016-5656-1.

[36] Y. Jin, L. Wang, Y. Shang, J. Gao, J. Li, Q. Jiang, X. Du, C. Ji, X. He, Characterization of Porous Micro-/nanostructured Co3O4 Microellipsoids, Elsevier Ltd, 2015, https://doi.org/10.1016/j.electacta.2015.10.187.

[37] K.F. Wadekar, K.R. N, S.A. W, Chemical synthesis of cobalt oxide (Co3O4) nanoparticles using Co) nanoparticles using Co-precipitation method, J. Phys. IV: JP 7 (1) (2017) 53–55, https://doi.org/10.1051/jp4:2001380.

[38] A. Ketema, D. Worku, N. Gabbiye, Engineering Co 3 O 4/MnO 2 nanocomposite materials for oxygen reduction electrocatalysis, Heliyon 7 (2021), e08076, https://doi.org/10.1016/j.heliyon.2021.e08076.

[39] N.R. Khalid, A. Batool, F. Ali, G. Nabi, M.B. Tahir, M. Rafique, Electrochemical study of Mo-doped Co3O4 nanostructures synthesized by sol–gel method, J. Mater. Sci. Mater. Electron. 32 (3) (2021) 3512–3521, https://doi.org/10.1007/s10854-020-05097-6.

[40] P.M. Kharade, J.V. Thombare, A.R. Babar, R.N. Bulakhe, S.B. Kulkarni, D.J. Salunkhe, Electrodeposited nanoflakes like hydrophilic Co3O4 as a supercapacitor electrode, J. Phys. Chem. Solid. 120 (2018) 207–210, https://doi.org/10.1016/j.jpcs.2018.04.035.

[41] A. Kucukarslan, E. Kus, E. Sarica, I. Akyuz, V. Bilgin, B. Demirselcuk, Improvement of structural , optical and magnetic properties of cobalt oxide thin films by doping with iron, Appl. Phys. A (2021) 1–9, https://doi.org/10.1007/s00339-021-04672-w.

[42] K.S. Kumar, N. Choudhary, D. Pandey, L. Hurtado, H.S. Chung, L. Tetard, Y. Jung, J. Thomas, High-performance flexible asymmetric supercapacitor based on rGO anode and WO3/WS2core/shell nanowire cathode, Nanotechnology 31 (43) (2020), https://doi.org/10.1088/1361-6528/aba305.

[43] N. Kumar, S. Bin Kim, S.Y. Lee, S.J. Park, Recent advanced supercapacitor: a review of storage mechanisms, electrode materials, modification, and perspectives, Nanomaterials 12 (20) (2022), https://doi.org/10.3390/nano12203708.

[44] Y. Lei, J. Li, Y. Wang, L. Gu, Y. Chang, H. Yuan, D. Xiao, Rapid microwave-assisted green synthesis of 3D hierarchical flower-shaped NiCo2O4 microsphere for high-performance supercapacitor, ACS Appl. Mater. Interfaces 6 (3) (2014) 1773–1780, https://doi.org/10.1021/am404765y.

[45] G. Li, M. Chen, Y. Ouyang, D. Yao, L. Lu, L. Wang, X. Xia, W. Lei, S.M. Chen, D. Mandler, Q. Hao, Manganese doped Co 3 O 4 mesoporous nanoneedle array for long cycle-stable supercapacitors, Appl. Surf. Sci. 469 (2019) 941–950, https://doi.org/10.1016/j.apsusc.2018.11.099.

[46] X. Li, F. Dong, N. Xu, T. Zhang, K. Li, J. Qiao, Co3O4/MnO2/Hierarchically porous carbon as superior bifunctional electrodes for liquid and all-solid-state rechargeable zinc-air batteries, ACS Appl. Mater. Interfaces 10 (18) (2018) 15591–15601, https://doi.org/10.1021/acsami.7b18684.

[47] Q. Liao, N. Li, S. Jin, G. Yang, C. Wang, All-solid-state symmetric supercapacitor based on Co3O4 nanoparticles on vertically aligned graphene, ACS Nano 9 (5) (2015) 5310–5317, https://doi.org/10.1021/acsnano.5b00821.

[48] Y. Liu, I. Murtaza, A. Shujia, H. Meng, Interfacial modification for heightening the interaction between PEDOT and substrate towards enhanced flexible solid supercapacitor performance, Chem. Eng. J. 379 (2020) 1–24, https://doi.org/10.1016/j.cej.2019.122326.

[49] Z. Liu, X. Tian, X. Xu, L. He, M. Yan, C. Han, Y. Li, W. Yang, Capacitance and Voltage Matching between MnO 2 Nanoflake Cathode and Fe 2 O 3 Nanoparticle Anode for High-Performance Asymmetric Micro-supercapacitors, 2017, https://doi.org/10.1007/s12274-017-1451-4.

[50] J. Lu, J. Li, J. Wan, X. Han, P. Ji, S. Luo, M. Gu, D. Wei, C. Hu, A facile strategy of in-situ anchoring of Co3O4 on N doped carbon cloth for an ultrahigh electrochemical performance, Nano Res. 14 (7) (2021) 2410–2417, https://doi.org/10.1007/s12274-019-3242-6.

[51] L. Ma, X. Shen, H. Zhou, Z. Ji, K. Chen, G. Zhu, High performance supercapacitor electrode materials based on porous NiCo2O4 hexagonal nanoplates/reduced graphene oxide composites, Chem. Eng. J. 262 (2015) 980–988, https://doi.org/10.1016/j.cej.2014.10.079.

[52] M. Manickam, V. Ponnuswamy, C. Sankar, R. Suresh, R. Mariappan, A. Chandra bose, J. Chandrasekaran, Structural, optical, electrical and electrochemical properties of Fe:Co3O4 thin films for supercapacitor applications, J. Mater. Sci. Mater. Electron. 28 (24) (2017) 18951–18965, https://doi.org/10.1007/s10854-017-7849-7.

[53] X. Min, M. Guo, L. Liu, L. Li, J. Gu, J. Liang, C. Chen, K. Li, J. Jia, T. Sun, Synthesis of MnO2 derived from spent lithium-ion batteries via advanced oxidation and its application in VOCs oxidation, J. Hazard Mater. 406 (2021), 124743, https://doi.org/10.1016/j.jhazmat.2020.124743.

[54] Z. Nate, A.A.S. Gill, R. Chauhan, R. Karpoormath, Polyaniline-cobalt oxide nanofibers for simultaneous electrochemical determination of antimalarial drugs: primaquine and proguanil, Microchem. J. 160 (PB) (2021), 105709, https://doi.org/10.1016/j.microc.2020.105709.

[55] J. Noh, C.M. Yoon, Y.K. Kim, J. Jang, High performance asymmetric supercapacitor twisted from carbon fiber/MnO2 and carbon fiber/MoO3, Carbon 116 (2017) 470–478, https://doi.org/10.1016/j.carbon.2017.02.033.

[56] M. Oza, M.J. Joshi, Hydrothermal synthesis of siderite nano-particles and characterizations, AIP Conf. Proc. 1837 (2017), https://doi.org/10.1063/1.4982121.

[57] M. Pal, R. Rakshit, A.K. Singh, K. Mandal, Ultra high supercapacitance of ultra small Co3O4 nanocubes, Energy 103 (2016) 481–486, https://doi.org/10.1016/j.energy.2016.02.139.

[58] T. Peng, X. Dai, Y. Zhang, P. Zheng, J. Wang, S. Wang, Z. Wang, Y. Zeng, J. Li, H. Jiang, Facile synthesis of SiO2@MnO2 nanocomposites and their applications on platforms for sensitively sensing antibiotics and glutathione, Sensor. Actuator. B Chem. 304 (2020), 127314, https://doi.org/10.1016/j.snb.2019.127314.

[59] T. Pettong, P. Iamprasertkun, A. Krittayavathananon, P. Sukha, P. Sirisinudomkit, A. Seubsai, M. Chareonpanich, P. Kongkachuichay, J. Limtrakul, M. Sawangphruk, High-performance asymmetric supercapacitors of MnCo2O4 nanofibers and N-doped reduced graphene oxide aerogel, ACS Appl. Mater. Interfaces 8 (49) (2016) 34045–34053, https://doi.org/10.1021/acsami.6b09440.

[60] A. Publication, C. Page, S. Komaba, Sodium-driven Rechargeable Batteries: an Effort towards a Future Energy Storage, 2020, https://doi.org/10.1246/cl.200568.

[61] M. Pudukudy, Z. Yaakob, Sol-gel synthesis, characterisation, and photocatalytic activity of porous spinel Co3O4 nanosheets, Chem. Pap. 68 (8) (2014) 1087–1096, https://doi.org/10.2478/s11696-014-0561-7.

[62] S. Ramesh, K. Karuppasamy, H.S. Kim, H.S. Kim, J.H. Kim, Hierarchical Flowerlike 3D nanostructure of Co3O4@MnO2/N-doped Graphene oxide (NGO) hybrid composite for a high-performance supercapacitor, Sci. Rep. 8 (1) (2018) 1–11, https://doi.org/10.1038/s41598-018-34905-7.

[63] R.S. Reena, A. Aslinjensipriya, M. Jose, S.J. Das, Investigation on structural, optical and electrical nature of pure and Cr-incorporated cobalt oxide nanoparticles prepared via co-precipitation method for photocatalytic activity of methylene blue dye, J. Mater. Sci. Mater. Electron. 31 (24) (2020) 22057–22074, https://doi.org/10.1007/s10854-020-04708-6.

[64] E. Samuel, A. Aldalbahi, M. El-Newehy, H. El-Hamshary, S.S. Yoon, Nickel ferrite beehive-like nanosheets for binder-free and high-energy-storage supercapacitor electrodes, J. Alloys Compd. 852 (2021), 156929, https://doi.org/10.1016/j.jallcom.2020.156929.

[65] M. Sharma, S. Sundriyal, A. Panwar, A. Gaur, Enhanced supercapacitive performance of Ni0.5Mg0.5Co2O4 flowers and rods as an electrode material for high energy density supercapacitors: rod morphology holds the key, J. Alloys Compd. 766 (2018) 859–867, https://doi.org/10.1016/j.jallcom.2018.07.019.

[66] Z. Sheikhi Mehrabadi, A. Ahmadpour, N. Shahtahmasebi, M.M. Bagheri Mohagheghi, Synthesis and characterization of Cu doped cobalt oxide nanocrystals as methane gas sensors, Phys. Scripta 84 (1) (2011), https://doi.org/10.1088/0031-8949/84/01/015801.

[67] S. Shin, M.W. Shin, Nickel metal–organic framework (Ni-MOF) derived NiO/C@CNF composite for the application of high performance self-standing supercapacitor electrode, Appl. Surf. Sci. 540 (2021), 148295, https://doi.org/10.1016/j.apsusc.2020.148295.

[68] A. Singh, D. Kumar, A. Thakur, B.S. Saini, Enhanced performance of Fe-doped manganese oxide films as supercapacitor electrodes, Bull. Mater. Sci. (2020), https://doi.org/10.1007/s12034-020-02139-x.

[69] L. Sun, Q. Fu, C. Pan, Mn3O4 embedded 3D multi-heteroatom codoped carbon sheets/carbon foams composites for high-performance flexible supercapacitors, J. Alloys Compd. 849 (2020), 156666, https://doi.org/10.1016/j.jallcom.2020.156666.

[70] M. Sundararajan, J. Vidhya, R. Revathi, M. Sukumar, V. Ravi, R. Rajkumar, M. Kamalakannan, C.S. Dash, H. Lohedan, R.J. Ramalingam, S. Arokiyaraj, Study of physical and magnetic properties of Mg:Co3O4 spinels using L-arginine as fuel, J. Ovonic Res. 17 (5) (2021) 479–486.

[71] S. Tian, B. Zhang, D. Han, Z. Gong, X. Li, Fe2O3/Porous carbon composite derived from oily sludge waste as an advanced anode material for supercapacitor application, Nanomaterials 12 (21) (2022) 3819, https://doi.org/10.3390/nano12213819.

[72] X. Wang, J. Fu, Q. Wang, Z. Dong, X. Wang, A. Hu, W. Wang, S. Yang, Preparation and electrochemical properties of co3o4 supercapacitor electrode materials, Crystals 10 (9) (2020) 1–11, https://doi.org/10.3390/cryst10090720.
[73] X. Wang, S. Yin, J. Jiang, H. Xiao, X. Li, A tightly packed Co3O4/C&S composite for high-performance electrochemical supercapacitors from a cobalt(III) cluster-based coordination precursor, J. Solid State Chem. 288 (2020), 121435, https://doi.org/10.1016/j.jssc.2020.121435.
[74] A.K. Worku, Engineering techniques to dendrite free Zinc-based rechargeable batteries, Front. Chem. (2022) 1–15, https://doi.org/10.3389/fchem.2022.1018461.
[75] A.K. Worku, D.W. Ayele, N.G. Habtu, Influence of nickel doping on MnO2 nanoflowers as electrocatalyst for oxygen reduction reaction, SN Appl. Sci. 3 (9) (2021), https://doi.org/10.1007/s42452-021-04746-7.
[76] A.K. Worku, D.W. Ayele, N.G. Habtu, Recent advances and future perspectives in engineering of bifunctional electrocatalysts for rechargeable zinc–air batteries, Mater. Today Adv. 9 (2021), 100116, https://doi.org/10.1016/j.mtadv.2020.100116.
[77] A.K. Worku, D.W. Ayele, N.G. Habtu, B.T. Admasu, G. Alemayehu, B.Z. Taye, T.A. Yemata, Energy storage technologies; recent advances, challenges, and prospectives, in: A.K. Bohre, P. Chaturvedi, M.L. Kolhe, S.N. Singh (Eds.), Planning of Hybrid Renewable Energy Systems, Electric Vehicles and Microgrid: Modeling, Control and Optimization, Springer Nature Singapore, 2022, pp. 125–150, https://doi.org/10.1007/978-981-19-0979-5_7.
[78] A.K. Worku, D.W. Ayele, N.G. Habtu, M.D. Ambaw, Engineering nanostructured Ag doped α-MnO2 electrocatalyst for highly efficient rechargeable zinc-air batteries, Heliyon 8 (10) (2022), e10960, https://doi.org/10.1016/J.HELIYON.2022.E10960.
[79] A.K. Worku, D.W. Ayele, N.G. Habtu, M.A. Teshager, Z.G. Workineh, Enhancing oxygen reduction reaction activity of ε-MnO2 nanoparticles via iron doping, J. Phys. Chem. Solid. 157 (June) (2021), https://doi.org/10.1016/j.jpcs.2021.110207.
[80] A.K. Worku, D.W. Ayele, N.G. Habtu, M.A. Teshager, Z.G. Workineh, Recent progress in MnO2-based oxygen electrocatalysts for rechargeable zinc-air batteries, Mater. Today Sustainability 13 (2021), https://doi.org/10.1016/j.mtsust.2021.100072.
[81] A.K. Worku, D.W. Ayele, N.G. Habtu, T.A. Yemata, Engineering Co3O4/MnO2 nanocomposite materials for oxygen reduction electrocatalysis, Heliyon 7 (9) (2021), e08076, https://doi.org/10.1016/j.heliyon.2021.e08076.
[82] K. Xiang, Z. Xu, T. Qu, Z. Tian, Y. Zhang, Y. Wang, M. Xie, X. Guo, W. Ding, X. Guo, Two dimensional oxygen-vacancy-rich Co3O4 nanosheets with excellent supercapacitor performances, Chem. Commun. 53 (92) (2017) 12410–12413, https://doi.org/10.1039/c7cc07515d.
[83] C.N. Yonti, P.K. Tsobnang, R.L. Fomekong, F. Devred, E. Mignolet, Y. Larondelle, S. Hermans, A. Delcorte, J.L. Ngolui, Green Synthesis of Iron-Doped Cobalt Oxide Nanoparticles from Palm Kernel Oil via Co-precipitation and Structural Characterization, 2021.
[84] J. Yu, X. Gao, Z. Cui, Y. Jiao, Q. Zhang, H. Dong, L. Yu, L. Dong, Facile synthesis of binary transition metal sulfide tubes derived from NiCo-MOF-74 for high-performance supercapacitors, Energy Technol. 7 (6) (2019), https://doi.org/10.1002/ente.201900018.
[85] T. Zhai, L. Wan, S. Sun, Q. Chen, J. Sun, Q. Xia, H. Xia, Phosphate ion functionalized Co3O4 ultrathin nanosheets with greatly improved surface reactivity for high performance pseudocapacitors, Adv. Mater. 29 (7) (2017) 1–8, https://doi.org/10.1002/adma.201604167.
[86] W. Zhou, G. Han, Y. Xiao, Y. Chang, W. Yuan, Y. Li, C. Liu, Y. Zhang, Polypyrrole doped with dodecyl benzene sulfonate electrodeposited on carbon fibers for flexible capacitors with high-performance, Electrochim. Acta 176 (2015) 594–603, https://doi.org/10.1016/j.electacta.2015.07.026.